remote sensing

MDPI

Article

Forest Aboveground Carbon Storage in the Three Parallel Rivers Region: A Remote Sensing and Machine Learning Perspective

Qin Xiang [1], Rong Wei [1], Chaoguan Qin [1], Lianjin Fu [2], Zhengying Li [1], Hailin He [1] and Qingtai Shu [1,*]

[1] College of Forestry, Southwest Forestry University, Kunming 650224, China; xq_001@swfu.edu.cn (Q.X.); wr0910@swfu.edu.cn (R.W.); qinchaoguan@swfu.edu.cn (C.Q.); lizhengying2306@dingtalk.com (Z.L.); hailinghe@swfu.edu.cn (H.H.)

[2] College of Soil and Water Conservation, Southwest Forestry University, Kunming 650224, China; fu_lj@swfu.edu.cn

* Correspondence: shuqt@swfu.edu.cn

Highlights

What are the main findings?

- We generated the first high-resolution (30 m), long-term (2003–2024) forest carbon dynamics map for the topographically complex Three Parallel Rivers Region using a machine learning framework.
- A net forest carbon increase of 67.05 Tg was revealed, providing empirical evidence for the effectiveness of regional ecological protection policies. We identified the interaction between temperature and population density as the dominant driver of carbon storage spatial heterogeneity.

What are the implications of the main findings?

- The study provides an effective reference for monitoring forest carbon sinks in globally complex terrains, which aids in supporting ecological management and conservation decision-making.
- It clarifies both the tangible carbon sequestration outcomes of ecological protection policies and the dominant driving mechanism of the "temperature–population density" interaction, offering a scientific basis for formulating future differentiated and targeted policies to enhance carbon sequestration.

Abstract

Accurate estimation of forest aboveground carbon (AGC) is crucial for understanding the carbon cycle and formulating climate policies, yet it remains challenging in complex mountainous regions. This study used machine learning framework to estimate the spatiotemporal dynamics of AGC in the Three Parallel Rivers region of China from 2003 to 2024. By integrating China's National Forest Continuous Inventory (NFCI) data with multispectral satellite imagery, we employed a two-stage feature selection strategy to identify key predictor variables. Among three ensemble algorithms tested, the Random Forest model achieved the optimal performance (R^2 = 0.74). The results indicated a net increase of 67.05 Tg in total AGC over the two decades, with a spatial pattern characterized by higher densities in the west and north. Geographical Detector analysis revealed that the driving forces were synergistic, with the interaction between temperature and population density exhibiting the most prominent explanatory capacity. This study provides a high-resolution (30 m) benchmark for AGC in a global biodiversity hotspot and underscores the critical role of ecological protection policies in enhancing carbon sequestration, offering valuable insights for managing similar mountain ecosystems worldwide.

Check for updates

Academic Editor: Huaqiang Du

Received: 21 January 2026
Revised: 22 February 2026
Accepted: 24 February 2026
Published: 2 March 2026

Copyright: © 2026 by the authors. Licensee MDPI, Basel, Switzerland. This article is an open access article distributed under the terms and conditions of the Creative Commons Attribution (CC BY) license.

Keywords: three parallel rivers region; carbon storage; machine learning; spatiotemporal variation; geodetector

1. Introduction

Against the backdrop of sustained growth in greenhouse gas emissions, global climate change has emerged as a major challenge threatening sustainable human development. In this context, the strategic role of forests as a "carbon pool" has become increasingly prominent, with their carbon sink function recognized as one of the most cost-efficient and effective methods for carbon sequestration and sink enhancement [1,2]. Research indicates that global forest carbon sinks offset nearly half of fossil fuel emissions from 1990 to 2019, playing a pivotal part in counteracting anthropogenic carbon emissions [3]. Among various forest carbon metrics, aboveground carbon stock (AGC), representing the total carbon stored in the vegetation's aboveground biomass, serves as the most direct indicator for assessing the carbon sequestration capacity and potential of forest ecosystems. The spatial and temporal dynamics of forest AGC are influenced by a complex interplay of biotic and abiotic factors, including but not limited to climatic conditions (e.g., temperature and precipitation), forest structural attributes (e.g., stand age, tree species composition, and canopy density), soil properties, topography, as well as direct and indirect human activities such as land-use change, forest management practices, and ecological protection policies [4–6]. Its accurate estimation is therefore crucial for formulating climate policies and guiding ecological conservation efforts [7].

The integration of satellite remote sensing technology with machine learning algorithms has significantly advanced the monitoring of spatiotemporal dynamics in AGC. For instance, Zhang Meng et al. utilized Landsat time-series data combined with the Random Forest algorithm to estimate AGC in parts of Hangzhou, China, achieving a model $R^2 = 0.73$. Their study found a 285% increase in total carbon stock between 2000 and 2018, despite a reduction in forest area [8]. Similarly, Kucuker Derya et al. analyzed the spatiotemporal patterns and driving factors of forest carbon dynamics in Hisar, Turkey, from 1973 to 2015 using forest inventory data, with a model $R^2 = 0.80$ [9]. They reported a 33.8% growth in total carbon storage, attributing it primarily to afforestation, cropland conversion to forests, and rural population decline [9]. However, prior studies have predominantly focused on economically advanced urban areas where data acquisition is relatively easier. In contrast, complex mountainous regions pose severe challenges due to harsh natural conditions, which hinder traditional ground surveys and data collection. This often leads to limitations in the consistency of spatial resolution, temporal coverage, and the ability of remote sensing-based estimation models to capture the intricate nonlinear relationships between features and AGC, consequently introducing uncertainties into regional carbon accounting [10–12]. Achieving high-precision AGC estimation in such geographically complex environments, characterized by significant spatial heterogeneity, remains a key challenge in current research [13,14].

In order to address the challenges of studying mountainous areas, an ideal model system has been proposed for the Three Parallel Rivers region in northwest Yunnan, China. This UNESCO World Heritage site is renowned for its dramatic altitudinal gradients (approximately 719 to 6619 m), unique canyon landforms, and rich biodiversity. Its complete vertical zonation spectrum makes it a microcosm of global mountainous ecological complexity [15,16]. This very complexity underscores the critical importance of systematic research on AGC dynamics in this region. Such studies are essential not only for understanding the local ecosystem's response to global changes but also for providing valuable

insights into the carbon cycle of other similar mountain ecosystems worldwide, such as the Himalayas and the Andes.

Therefore, this study intends to develop a robust machine learning framework for estimating AGC in the Three Parallel Rivers region by utilizing multi-year data from China's National Forest Continuous Inventory and Landsat series images. Adopting ensemble learning algorithms combined with feature selection strategies to optimize model performance, and integrating multi temporal remote sensing data with machine learning techniques to effectively reveal the long-term carbon storage dynamics and influencing mechanisms in the Three Parallel Rivers Region. The specific objectives of this study are: (1) to quantify the spatiotemporal changes in AGC from 2003 to 2024; (2) to identify key driving factors using geographical detectors; and (3) to provide a high-resolution (30 m) carbon stock distribution map.

The findings of this study are expected to provide a high-resolution, empirical evidence base for evaluating the effectiveness of past ecological protection policies in the Three Parallel Rivers Region. Furthermore, by identifying the key driving factors, they can offer scientific support for formulating differentiated and targeted forest management strategies to enhance carbon sequestration in similar complex mountain ecosystems globally.

2. Materials and Methods

2.1. Study Area

"The Three Parallel Rivers Region" is located in the northwestern part of Yunnan Province, China (98°00′–100°30′E, 25°30′–29°00′N). It lies at the convergence point of three major geographic regions: East Asia, South Asia, and the Qinghai–Tibet Plateau. This area serves as the southern extension of the Qinghai–Tibet Plateau, shifting toward the Yunnan-Guizhou Plateau, and is distinguished by the longitudinal valley structure of the Hengduan Mountains (Figure 1). The Nu River, Lancang River, and Jinsha River flow through the region. The study area encompasses eight major counties/cities: Deqin County, Fugong County, Gongshan Derung-Nu Autonomous County (Gongshan County), Lanping Bai-Pumi Autonomous County (Lanping County), Lushui City, Weixi Lisu Autonomous County (Weixi County), Shangri-La City, and Yulong Naxi Autonomous County (Yulong County). The terrain is mainly characterized by alternating distribution of high mountains and rivers, presenting a stepped feature of descending from northeast to southwest. The region exhibits significant altitude variation (approximately 760 to 6740 m above sea level), with temperatures gradually decreasing as elevation increases. It is dominated by a landscape of high mountains and deep gorges, and the predominant soil types are loam and sandy loam. The climate demonstrates significant vertical zonation, encompassing seven typical climate zones of the Northern Hemisphere. Consequently, the region boasts exceptionally rich biodiversity—hosting over 20% of China's higher plant species and 25% of its animal species on across merely 0.4% of the country's land area—and a complex variety of vegetation types.

2.2. Data Acquisition and Processing

2.2.1. Field Data Collection

The ground survey data for this study were derived from China's National Forest Continuous Inventory (NFCI). A total of 327 permanent monitoring plots, each measuring 800 m^2, located within Yunnan Province were utilized. The NFCI is conducted on a five-year cycle, and this analysis incorporated data from four complete survey campaigns undertaken in 2003, 2008, 2013, and 2018. In strict accordance with the "Technical Regulations for National Forest Continuous Inventory" and aligned with the specific objectives of this research, the focus was placed exclusively on forest aboveground carbon storage [17].

Therefore, carbon stocks residing in the litter layer and soil layer were excluded from the analysis. The aboveground carbon storage data were sourced directly from field measurements conducted at each individual plot.

The distribution of the 327 fixed monitoring sample plots in the Three Parallel Rivers area is shown in Figure 2. According to the statistics, the carbon storage of all sample plots ranged from 0.06 to 33.89 t in 2003, with an average of 6.21 t. The values were 0.15–30.85 t (average: 6.38 t) in 2008, 0.22–28.72 t (average: 6.46 t) in 2013, and 0.23–25.28 t (average: 6.73 t) in 2018.

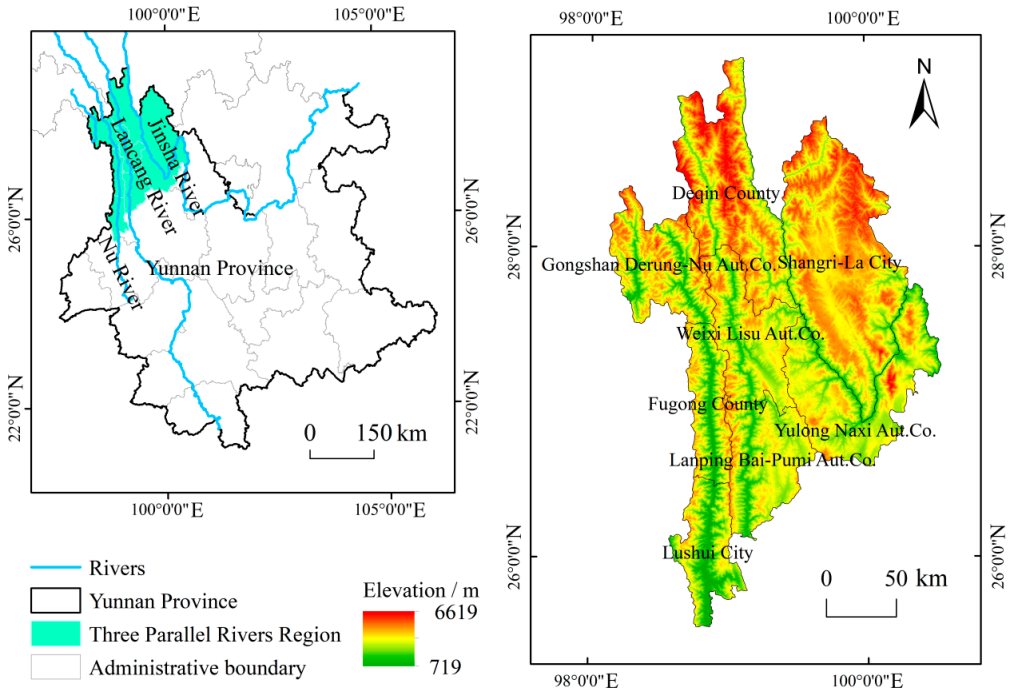


Figure 1. Geographical distribution diagram of the Three Parallel Rivers Region.

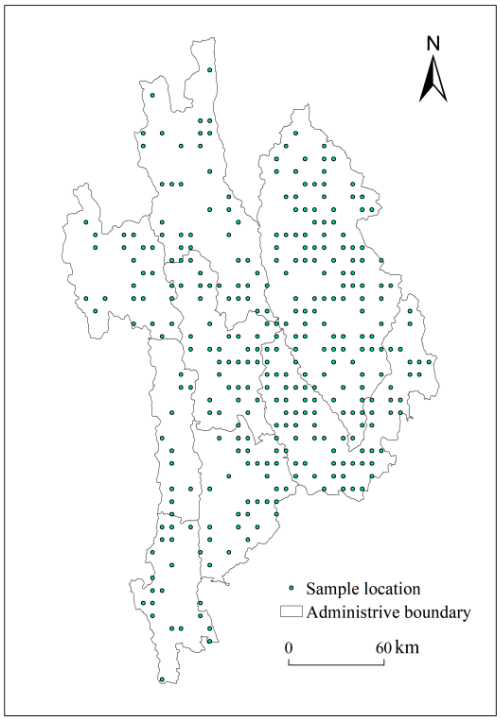


Figure 2. Spatial distribution map of sample plots.

2.2.2. Research Data

All datasets employed in the current research are summarized in Table 1. The Landsat-5 TM and Landsat-8 OLI remote sensing images were obtained from the Level 2 Collection 2 Tier 1 dataset. These datasets had undergone standardized radiometric and geometric corrections by the United States Geological Survey (USGS). After clipping and cloud removal, they were used for subsequent analysis. To ensure high data quality, all available satellite images from April to October within two years adjacent to the study years were selected. Median compositing was then applied to generate synthetic images with cloud cover below 10%. The Annual China Land Cover Dataset (CLCD) demonstrated an average overall accuracy (OA) of 79.30%, with the forest category achieving an F1-score of 85.49%. This dataset was used to construct multi-year forest distribution masks, effectively excluding non-forest areas. For monthly mean temperature, Fractional Vegetation Cover (FVC), and Normalized Difference Vegetation Index (NDVI) datasets, the monthly values were first extracted using an iterator. Subsequently, pixel-based statistical tools were employed to aggregate these monthly values, and multi-year climatic raster datasets were ultimately generated through temporal stacking.

Table 1. Data source and introduction.

Type	Dataset Name	Source	Resolution	Temporal Coverage
Remote sensing imagery	Landsat-5 TM Landsat-8 OLI	Google Earth Engine (accessed on 1 October 2025) (https://code.earthengine.google.com/)	30 m	2003, 2008, 2013, 2018, 2024
Administrative boundary	—	National Platform for CommonGeoSpatial Information Services (accessed on 5 October 2025) (https://www.tianditu.gov.cn/)	—	2024
Land use	Annual China Land Cover Dataset (CLCD)	ZENODO (accessed on 3 October 2025) (https://zenodo.org/records/15853565)	30 m	1985–2024
DEM	SRTM 30 m Digital Elevation Model	Geographic remote sensing ecological network platform (accessed on 3 October 2025) (www.gisrs.cn)	30 m	2024
Meteorological data	Monthly Mean Temperature	National Tibetan Plateau Scientific Data Center (accessed on 20 October 2025) (https://data.tpdc.ac.cn)	1 km	1901–2024
Nighttime light	Global NPP-VIIRS-like nighttime light data	Harvard Dataverse (accessed on 20 October 2025) (https://dataverse.harvard.edu/)	500 m	1992–2024
Population density	LandScan Global	ORNL LandScan Viewer (accessed on 23 October 2025) (https://landscan.ornl.gov/)	1 km	2003, 2008, 2013, 2018, 2024
FVC	Monthly Fractional Vegetation Cover in China	National Tibetan Plateau Scientific Data Center (accessed on 25 October 2025) (https://data.tpdc.ac.cn)	250 m	2000–2024
NDVI	Monthly Normalized Difference Vegetation Index	NASA Earthdata (accessed on 26 October 2025) (https://www.earthdata.nasa.gov/)	1 km	2000–2024

2.3. Research Methods

2.3.1. Extraction of Feature Variables

This study extracted remote sensing feature variables including original spectral bands, vegetation indices, principal component analysis factors, texture factors, and Tasseled Cap transformation factors, resulting in a total of 74 remote sensing factors. The original spectral bands were extracted from the preprocessed imagery, encompassing surface reflectance values from six bands: Blue (B2), Green (B3), Red (B4), Near-Infrared (NIR, B5), Shortwave Infrared 1 (SWIR1, B6), and Shortwave Infrared 2 (SWIR2, B7). Six vegetation indices—NDVI, GNDVI, DVI, MSAVI, RVI, and SAVI—were derived through linear operations on these bands. The first three bands (PC1, PC2, PC3) resulting from Principal Component Analysis (PCA) were extracted. Three components from the Tasseled Cap transformation—Brightness, Greenness, and Wetness—were also obtained. Texture features were calculated for the original six bands and PC1 using a 5 × 5 pixel window. Eight texture measures

(Mean, Variance, Homogeneity, Contrast, Dissimilarity, Entropy, Angular Second Moment, and Correlation) were extracted for each, yielding 56 texture factors in total.

2.3.2. Feature Variable Selection

To mitigate the computational complexity and overfitting risks associated with high-dimensional features, thereby improving the accuracy and stability of model estimation, this study adopted a two-stage feature selection strategy to optimize the initially extracted 74 remote sensing feature variables. In the first stage, Pearson correlation analysis was used to select features significantly correlated ($p < 0.05$) with AGC, reducing feature redundancy. Subsequently, the filtered feature subset was input into a Random Forest model. Based on the feature importance ranking, the key features were ultimately selected for constructing the final model [18,19].

2.3.3. Model Construction and Evaluation

Random Forest Regression (RFR) is an algorithm based on Bagging ensemble learning [20]. It generates multiple different data subsets from the training set through Bootstrap sampling, which are used to construct multiple decision trees in parallel. During the construction of each tree, a random subset of features is selected as candidates at each node split. The final output is obtained by taking the average of the prediction results from all the decision trees. This mechanism of dual randomness (data randomness and feature randomness) effectively reduces the model's variance, making it robust against overfitting.

Gradient Boosting Regression Tree (GBRT) is an algorithm based on Boosting ensemble learning [21]. Its core idea is to iteratively fit the residuals. Unlike the parallel construction of Random Forest, GBRT operates in a sequential manner. Each new decision tree is trained to learn the residual—the difference between the true values and the predicted values from the combination of models in the previous round. Through this step-by-step optimization, the model continuously reduces the prediction error.

eXtreme Gradient Boosting (XGBoost) is a high-performance gradient boosting algorithm [22]. Building upon the traditional gradient boosting framework, it introduces a second-order Taylor series expansion to approximate the loss function and incorporates regularization terms to control model complexity, thereby effectively improving prediction accuracy and preventing overfitting. During the decision tree construction process, this algorithm greedily finds the optimal split points by utilizing first and second-order derivative information and supports feature-level parallel computing to optimize training speed.

The machine learning algorithms employed in this study were implemented using third-party libraries on the Python 3.1.3 platform. The dataset was randomly split into a training subset and a validation subset in a 3:1 proportion. The model's accuracy and performance were evaluated using the Coefficient of Determination (R^2), Root Mean Square Error (RMSE), and Predictive Accuracy (P). The formulas are as follows:

$$R^2 = \frac{\sum_{i=1}^{n} (\hat{y}_i - \overline{y})^2}{\sum_{i=1}^{N} (y_i - \overline{y})^2} c \quad (1)$$

$$\mathrm{RMSE} = \sqrt{\frac{\sum_{\mathrm{i}=1}^{\mathrm{n}} (9\mathrm{y}_{\mathrm{i}} - \hat{\mathrm{y}}_{\mathrm{i}})^2}{\mathrm{n}}} \quad (2)$$

$$RRMSE = \frac{RMSE}{\overline{y}_i} \times 100\% \quad (3)$$

$$P = (1 - \frac{RMSE}{\overline{y}}) \quad (4)$$

In the formula: y_i is the measured value; $\hat{y}_i$ is the predicted value; $\overline{y}$ is the model predicted mean; n is the sample size.

2.3.4. Analysis of Spatiotemporal Changes in AGC

The spatiotemporal analysis of forest AGC primarily employs Moran's I, the Getis-Ord Gi*, and trend surface analysis. The Moran's I method is used to assess the extent of spatial clustering or dispersion of carbon storage across the entire study area, while the Getis-Ord Gi* method measures the concentration and differentiation of spatial units identified as either cold spots (low-value clusters) or hot spots (high-value clusters) [23,24]. The formulas are as follows:

$$I = \frac{n\sum_{i=1}^{n}\sum_{j=1}^{n} w_j(x_i - \overline{x})(x_j - \overline{x})}{n\sum_{i=1}^{n}(x_i - \overline{x})^2\left(\sum_{j=1}^{n}\sum_{i=1}^{n} w_j\right)} \quad (5)$$

$$G = \frac{\sum_{j=1}^{n} w_{ij}x_j - X\sum_{j=1}^{n} w_j}{\sqrt{\frac{n\sum_{j=1}^{n} w_j^2 - (\sum_{j=1}^{n} w_j)^2}{(n-1)}}} \quad (6)$$

where I represents Moran's Index. Its value ranges from -1 to 1. An $I > 0$ indicates a positive spatial autocorrelation, meaning that similar values (high—high or low—low) are clustered in space, and values closer to 1 suggest stronger clustering. An $I < 0$ indicates a negative spatial autocorrelation, meaning that dissimilar values are adjacent, and values closer to -1 suggest a stronger negative correlation. An $I = 0$ suggests a random spatial pattern with no autocorrelation. G represents the Getis-Ord Gi* statistic. n is the number of minimum spatial units in the study area. x_i and x_j are the attribute values of spatial units i and j, respectively. $\overline{x}$ is the average attribute value across the study area. $(x_i - \overline{x})$ denotes the deviation of the attribute value in the *ith* spatial unit from the mean. w_{ij} is the spatial weight matrix defining the relationship between units i and j.

Trend surface analysis can reveal the overall spatial variation trends and patterns of forest carbon storage. This method proceeds from the perspective of spatial interpolation. Based on extensive discrete point information, it converts two-dimensional spatial point data into a three-dimensional visually smooth curve to derive the final distribution characteristics.

$$Z_i(x_i, y_i) = T_i(x_i, y_i) + \varepsilon_i \quad (7)$$

where (x_i, y_i) represents the geographical coordinates. $Z_i(x_i, y_i)$ is the attribute value at the *ith* position. $T_i(x_i, y_i)$ is the fitted value from the trend surface. ε_i is the residual, representing the deviation between the observed value and the fitted result.

2.3.5. Driver Factor Analysis Using Geodetector

This study adopted the Geodetector model to analyze the driving forces of carbon storage changes in the Three Parallel Rivers Region. The core of this approach lies in measuring the spatial heterogeneity of geographical elements and elucidating their underlying driving factors. Utilizing both the factor detector and interaction detector modules, and based on the spatial heterogeneity theory, the model assesses the similarity between independent variables and the dependent variable [25]. The formula are as follows:

$$q = 1 - \frac{1}{N\sigma^2}\sum_{h=1}^{L} N_h\sigma_h^2 hL \ (h = 1, 2, \ldots, L) \quad (8)$$

where q represents the explanatory power of the independent variable X (driving factor) on the dependent variable Y; L denotes the number of classifications or strata of X or Y; N_h and N indicate the sample sizes in stratum hand the entire study area, respectively; σ_h^2

and σ^2 represent the variances of the dependent variable within stratum hand the entire study area, respectively. The value of q ranges between 0 and 1.

2.3.6. Continuous Factor Discretization

Using the Python platform, the q of each driving factor were calculated under different classification methods (geometric interval, natural breaks, equal interval, and quantile classification) and class numbers (4~9). The classification method and number of classes that yielded the highest q for each driving factor were selected to achieve optimal spatial discretization. The final discretization parameters determined are shown in Table 2.

Table 2. Discretization results of continuous factors.

Driving Factor	Classification Method	Class Number
FVC	Quantile	8
NDVI	Natural breaks	8
Temperature	Geometric interval	9
Nighttime light	Geometric interval	4
Population density	Quantile	8

3. Results

3.1. Changes in Forest Area

Based on the CLCD, forested areas within the Three Parallel Rivers Region were extracted for the years 2003, 2008, 2013, 2018, and 2024 (Figure 3). The results reveal a general increasing trend in forest area within the region from 2003 to 2024, with a net gain of 713.06 km^2. Among the various administrative district in the study area, Shangri-La City contained the largest forest area, accounting for over 25% of the total, followed by Deqin County and Yulong Naxi Autonomous County. Overall, the spatial and temporal changes in forest area were not pronounced, maintaining a relatively stable state across the different periods (Table 3).

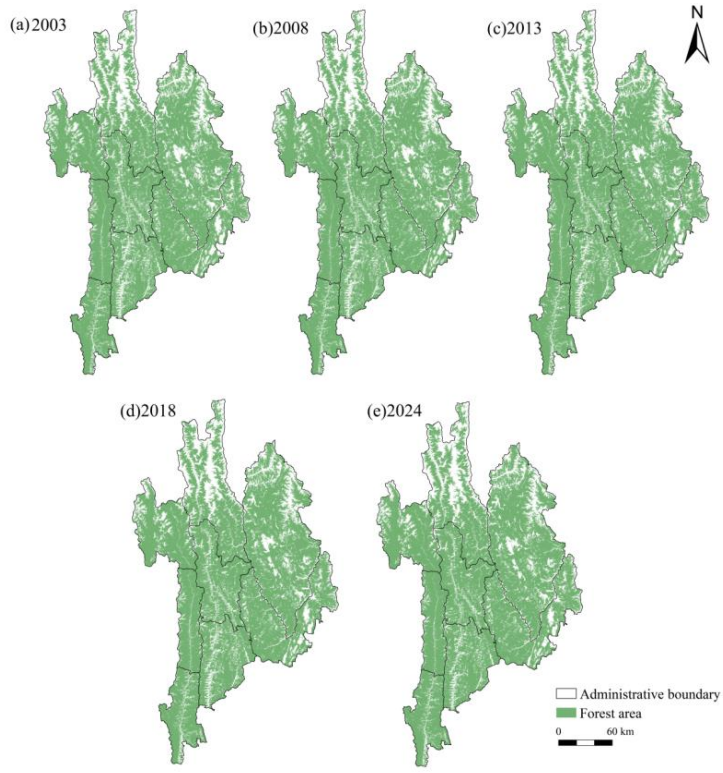


Figure 3. Changes in forest area during different periods.

Table 3. Statistics of forest area in various administrative district.

District	2003		2008		2013		2018		2024	
	Area/km^2	Proportion/%	Area/km^2	Proportion/%	Area/km^2	Proportion/%	Area/km^2	Proportion/%	Area/km^2	Proportion/%
Deqin County	4307.20	12.91	4340.12	12.93	4384.92	13.01	4394.71	13.02	4411.54	12.95
Fugong County	2444.86	7.33	2464.09	7.34	2463.72	7.31	2450.94	7.26	2476.64	7.27
Gongshan County	3514.05	10.53	3542.81	10.56	3559.58	10.56	3557.80	10.54	3564.75	10.46
Lanping County	3435.65	10.30	3438.54	10.25	3472.32	10.30	3512.98	10.41	3608.74	10.59
Lushui City	2723.54	8.16	2724.31	8.12	2700.90	8.01	2701.10	8.00	2728.09	8.01
Weixi County	3632.45	10.89	3676.85	10.96	3691.82	10.95	3689.68	10.93	3776.74	11.09
Shangri-La City	8382.83	25.13	8439.99	25.15	8504.79	25.23	8513.99	25.23	8544.79	25.08
Yulong County	4916.47	14.74	4931.95	14.70	4937.50	14.64	4924.56	14.59	4958.82	14.55

3.2. Feature Variable Screening Results

A Pearson correlation analysis was conducted between the 74 extracted feature variables and the carbon storage values. The correlation coefficients for all features ranged from −0.33 to 0.23 (Figure 4). Subsequently, the autocorrelation among the variables was calculated. To reduce informational redundancy, variables with an autocorrelation greater than 0.9 were eliminated, resulting in a pre-selected set of 36 variables. This pre-selected variable set was then input into a Random Forest regression model for feature importance ranking. The importance contributions of the features ranged from 0.42% to 13.18% (Figure 5). To identify key variables for constructing a high-quality model, a threshold of 5% was applied, which determined six feature variables: B4_Mean (13.18%), B4 (11.56%), B6_Mean (11.06%), B7 (5.37%), B2_Mean (5.17%), and B5_Variance (5.02%).

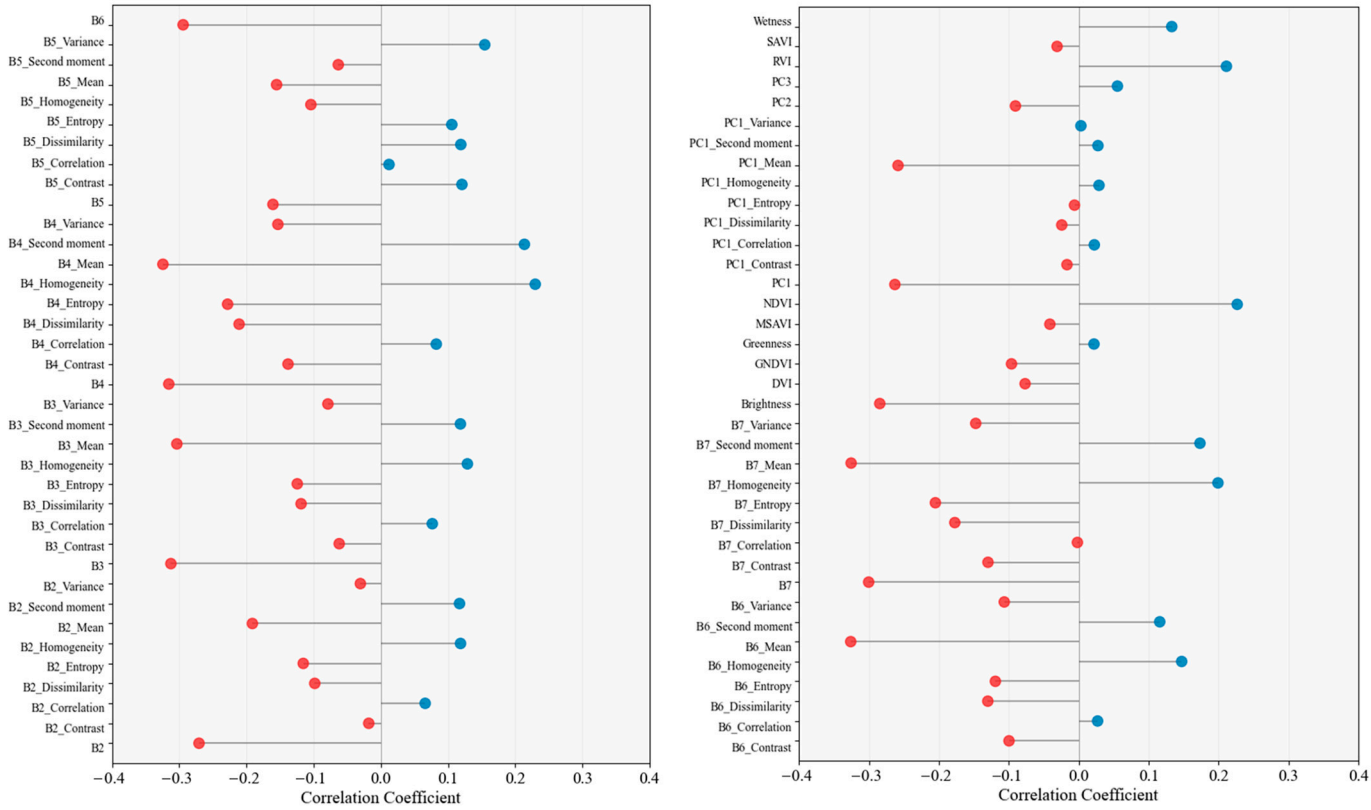


Figure 4. Pearson correlation coefficient between feature variables and AGC. Blue indicates positive correlation coefficients, while red indicates negative values.

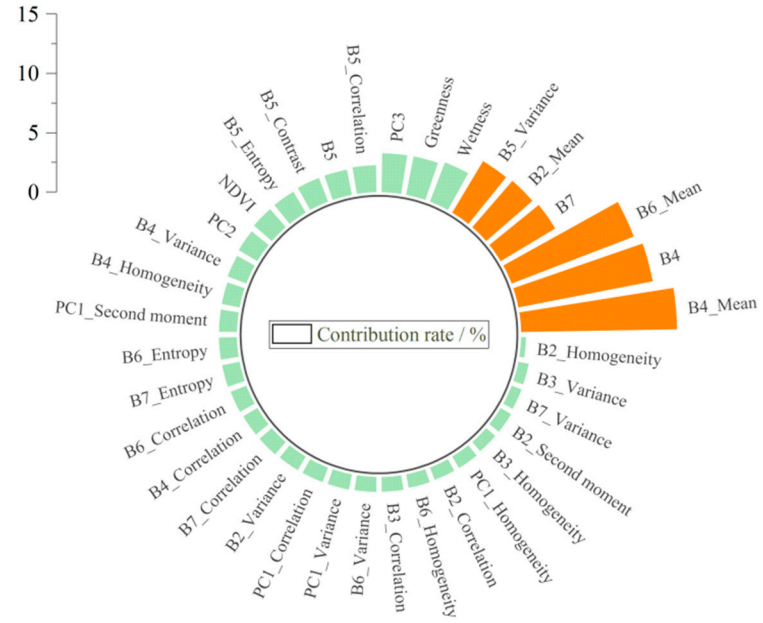


Figure 5. Contribution rate of each feature variable.Orange in the figure indicates contribution rate > 5%.

3.3. AGC Model Performance

The variables B4_Mean, B4, B6_Mean, B7 and B2_Mean were used as the independent variable set, while the field-measured AGC served as the dependent variable. The dataset was randomly split into training and testing sets in a ratio of 3:1. The RF, GBRT, and XGBoost algorithms were applied, and their performance was validated using the test set. The results are shown in Figure 6 and Table 4. In the remote sensing estimation of forest AGC, the RF model achieved the best performance, with R^2 = 0.74, RMSE = 3.05 t·hm^{-2}, RRMSE = 29.0%, and Predictive Accuracy (*P*) = 77.37%, demonstrating strong predictive capability and high fitting accuracy. The GBRT model ranked second, followed by the XGBoost model. But all models have a consistent systematic underestimation bias problem, and the predicted AGC values are lower than the observed values.

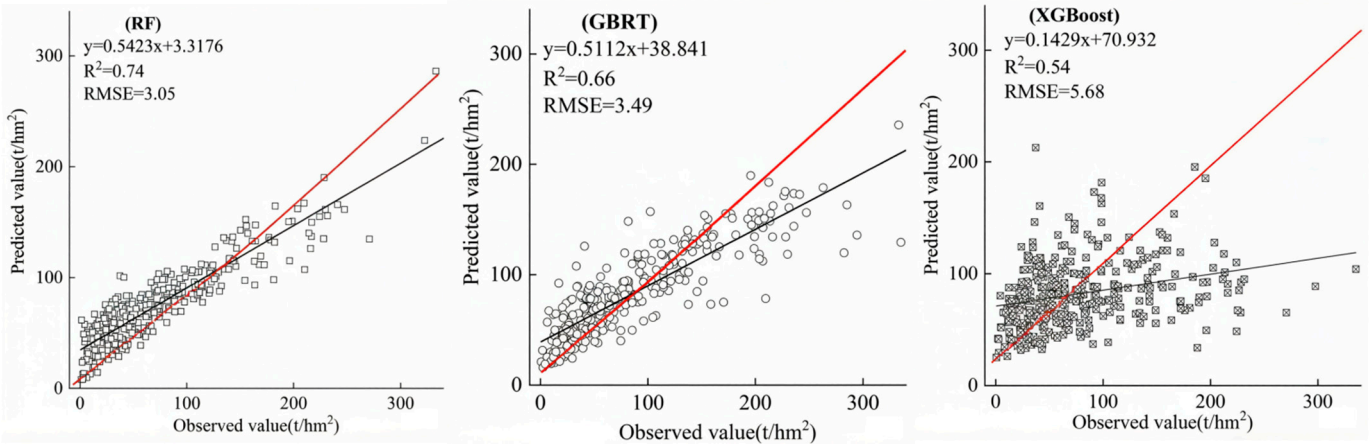


Figure 6. Comparison of model accuracy based on different algorithms. Red Line:A reference line indicating complete consistency between predicted and observed values. Black line: A linear fit that displays the actual trend of data.

Table 4. Accuracy evaluation of different models.

Modelling Algorithm	Training Set			Test Set		
	R^2	RMSE/t·hm^{-2}	RRMSE/%	R^2	RMSE/t·hm^{-2}	RRMSE/%
RF	0.83	2.41	23.0%	0.74	3.05	29.0
GBRT	0.78	2.87	27.3	0.66	3.49	33.2
XGBoost	0.61	4.92	46.9	0.55	5.68	54.1

3.4. Spatiotemporal Dynamics of AGC

Based on model inversion, the total AGC in the Three Parallel Rivers Reigon from 2003 to 2024 was estimated to be between 222.19 and 289.24 Tg. Overall, carbon storage showed a fluctuating but increasing trend, with a net increase of 67.05 Tg over the recent 20-year period. By year, AGC was highest in 2024, reaching 289.24 Tg, with an average carbon density of 83.57 t·hm^{-2}. The total carbon storage for 2003, 2008, 2013, and 2018 was 222.19, 217.70, 256.24, and 234.03 Tg, respectively, with corresponding average carbon densities of 79.14, 75.78, 89.13, and 81.58 t·hm^{-2}.

To systematically analyze the spatiotemporal distribution characteristics of AGC, the carbon density values (C_a) derived from the five periods of inversion results were classified into five gradient intervals: $C_a \leq 30$, $30 < C_a \leq 60$, $60 < C_a \leq 90$, $90 < C_a \leq 120$, and $C_a > 120$ t·hm^{-2} (Figure 7). Using pixels as the basic statistical units, the spatial proportion distribution of these gradient intervals for each period was calculated (Table 5). Analysis across different administrative districts revealed notable spatial changes in Gongshan County, Shangri-La City, Fugong County, Lushui City, and Lanping County. Gongshan County, Fugong County, and Shangri-La City consistently exhibited high-density carbon storage aggregation across all periods, significantly higher than other areas. In contrast, Lushui City and Lanping County still had substantial areas with negligible carbon storage from 2003 to 2018, but showed significant improvement by 2024.

From the perspective of carbon density gradients, the average carbon density in the Three Parallel Rivers Region from 2003 to 2024 followed a trend of decrease, increase, decrease, and then increase again, peaking in 2013. The pattern of carbon storage changes has gradually evolved from early local fluctuations and alternating changes to later widespread increases and spatially continuous changes (Figure 8). Areas with a carbon density exceeding 120 t·hm^{-2} accounted for 15.95% in 2013, significantly higher than in other years. Across all years in the study area, the proportion of areas with carbon density between $60 < C_a \leq 90$ t·hm^{-2} was consistently the highest, reaching 49.14% in 2024. Conversely, areas with carbon density below 30 t·hm^{-2} accounted for the smallest proportion, only 1.65% in 2024. This indicates a reduction in the proportion of low-carbon storage areas across the region, suggesting a progressive, qualitative increase in carbon storage.

The study further constructed spatial trend surfaces of carbon storage from 2003 to 2024 (Figure 9). The spatial pattern for all five periods was generally characterized by being higher in the west and lower in the eastern region, while being higher in the northern area and lower in the southern area. This macro-scale pattern aligns with the spatial distribution of high carbon storage areas (shown in red and orange in Figure 7), which were predominantly concentrated in the western and northern parts of the study area. This distribution is likely influenced by regional geo-environmental factors, such as the contiguous mountainous terrain in the west and north, and areas of intensive human activity in the eastern and southern parts.

A global spatial autocorrelation analysis was performed with townships serving as the basic spatial units. The results indicated that among the five study periods, only the years 2003 and 2008 yielded Global Moran's I values that were statistically significant ($p \leq 0.05$), demonstrating a spatially positive autocorrelation pattern. This suggests that the forest

aboveground carbon storage within the study area was not randomly distributed in its earlier stages. In contrast, the spatial distributions of carbon storage in 2013, 2018, and 2024 were closer to random, without forming significant clustering patterns. Consequently, an in-depth cold spot and hot spot analysis (Figure 10) was performed only for the years 2003 and 2008, which exhibited significant spatial dependence. From 2003 to 2008, the cold and hot spots were primarily located in western Gongshan County, southern Deqin County, northern Shangri-La City, and central Lanping County. The high-value clusters of carbon storage showed a trend of expansion and consolidation, while the low-value clusters exhibited no significant change. Throughout the entire study period from 2003 to 2024, the carbon storage level increased across most of the study area, even during years when overall spatial clustering was not statistically significant. This implies that the dominant factors driving the increase in carbon storage operated across the entire region. This widespread enhancement likely contributed to a reduction in local spatial heterogeneity, which in turn led to the non-significant global spatial autocorrelation observed in the later years.

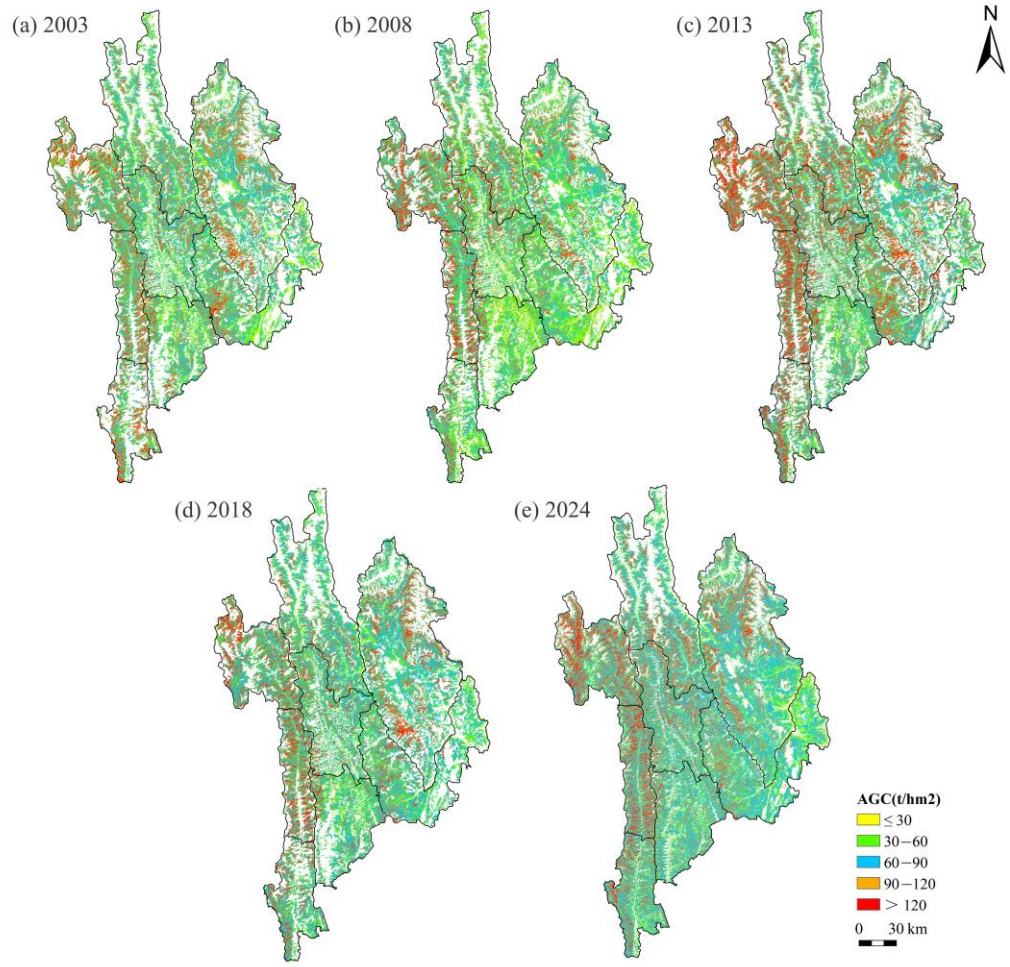


Figure 7. Distribution of AGC in forests at different periods.

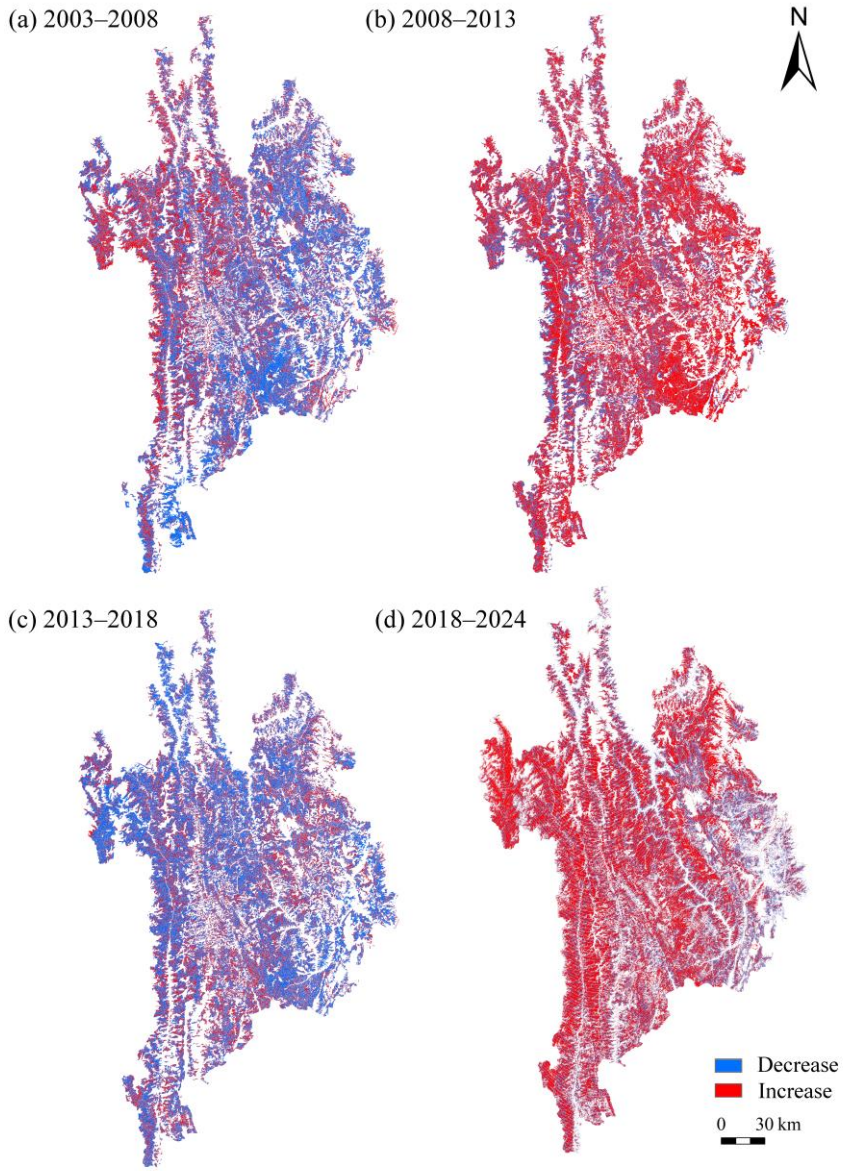


Figure 8. Annual changes of carbon storage.

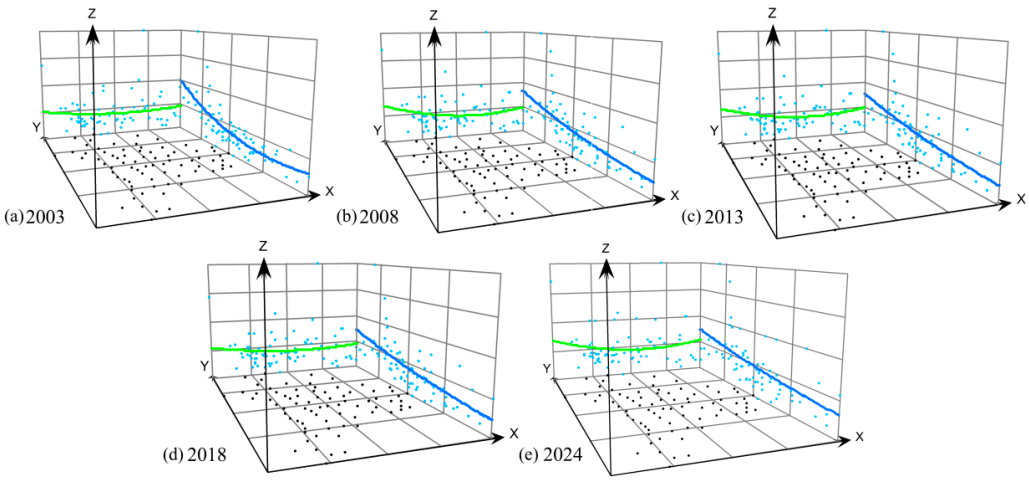


Figure 9. Spatial trend of AGC from 2003 to 2024. The green curve/points represent the distribution or trend of carbon storage values along the east-west direction, while the blue curve/points represent the distribution or trend of carbon storage values along the north-south direction.

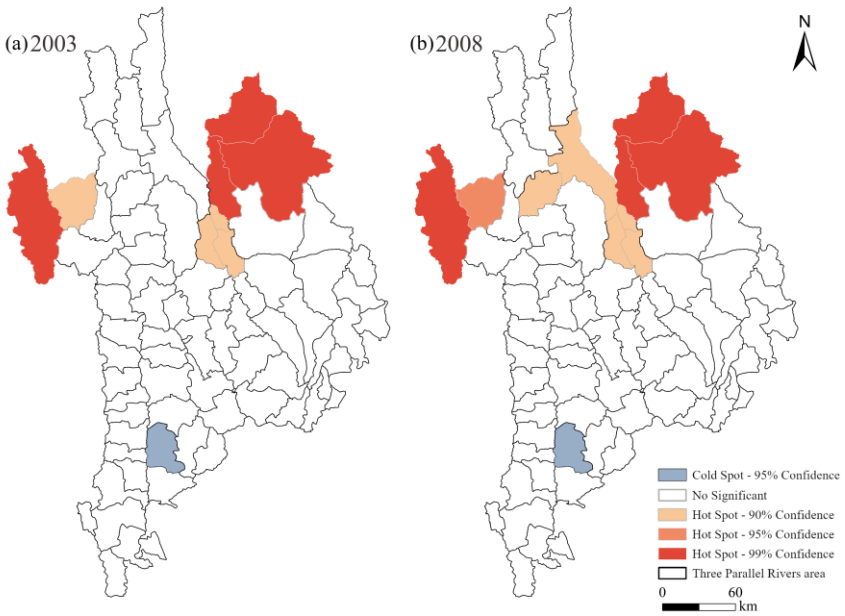


Figure 10. Analysis of AGC cold and hot spots from 2003 to 2008.

Table 5. Proportion of carbon storage per unit area at different levels.

Carbon Storage per Unit Area (C_a)/t·hm^{-2}	Proportion in Different Periods/%				
	2003	2008	2013	2018	2024
≤30	5.15	6.21	2.58	2.55	1.65
30–60	19.14	29.45	14.43	20.40	16.81
60–90	41.81	36.78	40.73	45.93	49.14
90–120	26.06	18.69	26.31	20.60	21.89
>120	7.84	8.86	15.95	10.51	10.51

3.5. Results of Geodetector Analysis

Single-factor driver detection results (Table 6) show that temperature had a relatively prominent explanatory power for AGC across different years. However, the overall explanatory power of single factors was relatively low (q < 25%; a q-value > 25% is generally considered indicative of strong explanatory power), suggesting that individual factors alone have limited ability to explain the spatial variation in AGC.

Interaction detection results (Table 7) indicate that, across all periods, the interactive effects between different factors enhanced the explanatory power for AGC compared to that of individual factors. All driver factor interactions demonstrated either bilinear enhancement or nonlinear enhancement, with no instances of weakening or independent effects. This reveals that the AGC in the study area exhibits multi-factor synergistic driving characteristics. Between 2003 and 2018, the interaction between population density and temperature was the strongest (reaching a maximum of 55.17%), while in 2024, the interaction between FVC and temperature was the most significant (38.81%). This indicates that the influence of temperature on AGC in this study significantly varies depending on regional population density or FVC levels.

Table 6. Single-factor detection analysis results.

Explanatory Power	Year	FVC	Nighttime Light	Population Density	Temperature	NDVI
q/%	2003	1.07	0.43	7.91	17.73	2.98
	2008	5.37	0.61	6.68	14.76	9.28
	2013	2.28	0.60	5.47	11.44	1.74
	2018	4.51	1.38	6.33	18.77	20.03
	2024	2.18	1.43	3.42	14.42	0.66

Table 7. Interaction factor detection analysis results.

Year	Driving Factor	Explanatory Power	FVC	Nighttime Light	Population Density	Temperature	NDVI
2003	FVC	*q*/%	1.07	—	—	—	—
	Nighttime light		3.71	0.43	—	—	—
	Population density		14.73	9.27	7.91	—	—
	Temperature		24.80	19.02	55.17	17.73	—
	NDVI		8.01	4.80	17.36	35.30	2.98
2008	FVC	*q*/%	5.37	—	—	—	—
	Nighttime light		6.85	0.61	—	—	—
	Population density		15.82	8.03	6.68	—	—
	Temperature		32.54	16.25	48.05	14.76	—
	NDVI		17.09	10.97	22.67	42.07	9.28
2013	FVC	*q*/%	2.28	—	—	—	—
	Nighttime light		5.31	0.60	—	—	—
	Population density		14.31	6.88	5.47	—	—
	Temperature		31.89	12.93	45.83	11.44	—
	NDVI		8.86	3.73	8.00	20.50	1.74
2018	FVC	*q*/%	4.51	—	—	—	—
	Nighttime light		7.06	1.38	—	—	—
	Population density		13.65	9.07	6.33	—	—
	Temperature		46.49	23.45	51.88	18.77	—
	NDVI		27.40	22.66	27.44	34.00	20.03
2024	FVC	*q*/%	2.18	—	—	—	—
	Nighttime light		6.86	1.43	—	—	—
	Population density		19.58	9.64	3.42	—	—
	Temperature		38.81	17.50	21.97	14.42	—
	NDVI		6.16	3.34	6.05	20.70	0.66

4. Discussion

Since 1999, the Yunnan Provincial Government has successively promulgated a series of management regulations. Over more than 20 years of continuous protection has provided crucial support for the ecological construction of the Three Parallel Rivers area and achieved remarkable results. This study systematically revealed the spatiotemporal evolution trends and driving factors of AGC in the Three Parallel Rivers area from 2003 to 2024.

Three algorithms were used for regional AGC modeling, and the results indicated that the RF model performed best. Yang et al. estimated the carbon sink intensity of Shangri-La using Landsat data and an RF model optimized with a Genetic Algorithm (GA), achieving an R^2 of 0.83 [26]. Wang et al. modeled the aboveground biomass of coniferous and broad-leaved mixed forests in Yunnan Province using Landsat series data and RF, with a model R^2 of 0.71 [19]. Without distinguishing tree species, our model achieved an accuracy of R^2 = 0.74 and RMSE = 3.05, which aligns with the results of relevant studies, confirming the applicability of the RF algorithm for estimating forest carbon storage in this complex mountainous region. The systematic underestimation bias problem of the model may be attributed to several factors. First, signal saturation in

optical sensors (e.g., Landsat) is a well-known limitation in dense, high-biomass forests, where spectral reflectance ceases to increase linearly with increasing biomass, leading to an underestimation plateau [27,28]. Second, potential under-representation of the highest biomass forest plots in the NFCI training data could bias the model, preventing it from fully learning the spectral characteristics of these extreme values [29]. Third, machine learning regression models inherently tend to compress predictions towards the mean to minimize overall error, which can dampen the prediction of high values [30].

The total AGC estimated for the five periods in this study ranged from 222.19 to 289.24 Tg, with an average carbon density of 75.78~83.57 t·hm^{-2}. In comparison, Tu et al. estimated the total forest vegetation carbon storage in Yunnan Province in 2018 to be 1050 Tg, with an average carbon density of 44.96 t·hm^{-2} [31]. Fan et al. estimated the aboveground carbon storage in northwestern Yunnan Province for 2022, reporting a total of 371.7 Tg and an average density of 42.64 t·hm^{-2} [32]. Consequently, the carbon density in the Three Parallel Rivers area is significantly higher than in other parts of Yunnan Province. This can be attributed to the region's unique climate and environment, coupled with strong protection policies, which have collectively fostered the persistence of high-carbon-density forests.

In terms of spatiotemporal dynamics, the forest area in the Three Parallel Rivers region showed a consistent increasing trend from 2003 to 2024, with a cumulative increase of 2.14%. However, the overall AGC exhibited a fluctuating upward trend. This pattern likely results from the combined effects of various factors, including inherent forest growth dynamics, external environmental changes, and human activities. This fluctuation pattern may be due to the following reasons: firstly, the characteristically low carbon storage in newly established restoration forests; secondly, the plateauing of carbon sequestration rates as forests reach maturity; and thirdly, the significant carbon pool alterations caused by large-scale tree mortality due to extreme climate events and subsequent regenerative processes [33–35]. Spatially, the distribution of AGC consistently showed a pattern of "higher in the west and lower in the east, higher in the north and lower in the south." High-value areas were concentrated in several nature reserves (e.g., Gaoligong Mountain National Nature Reserve, Hongshan Scenic Area, Qianhu Mountain Scenic Area), which directly confirms the effectiveness of mandatory protection policies in maintaining forest carbon sink functions. In contrast, low-value areas overlapped with urban zones, which have long served as agricultural and economic hubs, revealing the tension between economic development and ecological protection and providing a scientific basis for regional coordinated sustainable development. This spatial pattern reflects the combined shaping influence of the natural environment and human activities [36].

Global spatial autocorrelation analysis revealed a significant positive spatial correlation only in 2003 and 2008. This pattern likely stemmed from the initially incomplete coverage of ecological protection policies in the early stages, which allowed local factors to exert a stronger influence on AGC, resulting in pronounced spatial heterogeneity. As the scope of protection expanded and management measures intensified, the dominant drivers of AGC increase (such as regional conservation policies) began to affect the entire study area. While promoting a widespread rise in AGC, this process also mitigated local heterogeneity, thereby leading to non-significant global spatial autocorrelation in later periods. This spatial–temporal evolution profoundly reflects the decisive role of ecological policies in shaping the distribution pattern of AGC [37]. The geographical detector results indicated that the explanatory power of all single factors for the spatial differentiation of ACS was relatively weak, with only mean annual temperature having a relatively strong explanatory power. This is likely because the complex mountainous terrain with significant vertical drop creates substantial temperature differences, which to some extent influence the spatial

differentiation of AGC over long time series [38]. Although the independent explanatory power of single factors was limited, the interaction analysis using the geographical detector revealed a more complex driving mechanism. The interaction detection results showed that the explanatory power of the interaction between different factors in each period was enhanced compared to single factors. Specifically, the interaction effect of mean annual temperature with population density or FVC on AGC was significantly higher than other interactive factors. This phenomenon is related to the increased sensitivity of complex mountain ecosystems under climate change [19]. In the relatively flat southern regions, population density was the main driver of AGC changes, whereas in the northern regions with significant natural constraints, climatic factors like mean annual temperature played a more prominent role.

The results validate the applicability and reliability of the Random Forest model for estimating forest carbon storage in complex terrain. More importantly, from the perspective of the carbon cycle, this study quantifies the carbon sequestration benefits resulting from ecological protection efforts over the past two decades in the Three Parallel Rivers World Heritage Site. When facing natural disturbances like extreme climate events, consistent and robust protection policies and ecological engineering have effectively promoted forest area recovery and enhanced carbon storage accumulation in certain areas, thereby consolidating the region's ecological function as a significant carbon sink.

This study has several limitations that should be acknowledged. First, the reliance on optical remote sensing imagery (Landsat) may lead to an underestimation of AGC in dense forest stands due to signal saturation, a common challenge in high-biomass areas. Second, the spatial resolution of some driving factor datasets (e.g., NDVI data, population density at 1 km) is relatively coarse for the complex mountainous terrain. While suitable for regional-scale analysis, this resolution may not fully capture fine-scale local variability, potentially introducing uncertainty into the Geodetector analysis and the final high-resolution AGC maps. Third, the machine learning model was trained on ground data from 2003 to 2018. Consequently, the 2024 AGC map is a projection based on historical relationships, and its estimates carry higher uncertainty due to the absence of independent ground validation data for that specific year. Finally, the set of potential drivers, while informative, was not exhaustive. Other factors, such as soil properties, detailed disturbance history, and species composition, were not included, which may limit a comprehensive understanding of the driving mechanisms.

5. Conclusions

In conclusion, our analysis of the Three Parallel Rivers Region demonstrates a significant enhancement of its forest carbon sink function between 2003 and 2024, attributable to effective ecological protection policies. The region witnessed a net gain of 713.06 km^2 in forest area and an increase of 67.05 Tg in AGC stock. Peaks in carbon storage occurred in 2013 and 2024, with the highest average carbon density (89.13 $t \cdot hm^{-2}$) observed in 2013. Spatially, the AGC distribution pattern was characterized by higher densities in the western and northern parts, particularly within natural reserves, yet a generalized improvement was observed across the entire region, underscoring the critical role of policy-driven human intervention.

Furthermore, our investigation uncovered a multi-factor synergistic driving mechanism for AGC dynamics. While individual factors like temperature exhibited limited explanatory power ($q < 25\%$), their interactions considerably enhanced the interpretation (up to 55.17%), revealing that the coupling of climate change and human activities is the primary driver of carbon stock variation. The weakening of global spatial autocorrelation after 2008, coinciding with the widespread application of conservation policies,

suggests a reduction in local heterogeneity. This study provides a valuable high-resolution (30 m) benchmark for mountain ecosystem carbon cycle research and emphasizes the importance of sustained monitoring to mitigate uncertainties associated with extreme climate disturbances.

Future research should focus on enhancing the robustness and mechanistic depth of AGC estimation in complex terrains. A primary direction is the integration of multi-source remote sensing data. Combining optical imagery with Synthetic Aperture Radar (SAR) and LiDAR data could mitigate the saturation issue and provide direct vertical structure information, significantly improving estimation accuracy. Secondly, the understanding of driving mechanisms can be refined by incorporating higher-resolution datasets (e.g., for microclimate and anthropogenic activities) and employing spatiotemporal models like Geographically and Temporally Weighted Regression (GTWR) to reveal the heterogeneous effects of drivers across space and time.

Author Contributions: Conceptualization, Q.X. and Q.S.; methodology, Q.X., R.W. and C.Q.; software, R.W., L.F. and Q.X.; formal analysis, Q.X., R.W. and Z.L.; investigation, Q.X., C.Q. and H.H.; resources, Q.S., R.W. and Z.L.; data curation, Q.X.; writing—original draft preparation, Q.X.; writing—review and editing, R.W., Q.S., Z.L., L.F. and C.Q.; visualization, Q.X., L.F. and H.H.; supervision, Q.S. and Z.L.; project administration, Q.X. and Q.S.; funding acquisition, Q.S. All authors have read and agreed to the published version of the manuscript.

Funding: This study was supported by the Joint Agricultural Project of Yunnan Province [202301BD070001-002], Forestry Discipline and Key Laboratory Open Fund Project [LXXK-2025D1], National Natural Science Foundation of China [31860205], the Yunnan Provincial Department of Education Postgraduate Tutor Team Project [503250109], Yunnan Provincial Department of Education's Scientific Research Fund Project [2025Y0847].

Data Availability Statement: Data will be made available on request.

Conflicts of Interest: The authors declare no conflicts of interest.

Abbreviations

The following abbreviations are used in this manuscript:

AGC	Aboveground carbon
NFCI	National Forest Continuous Inventory
USGS	United States Geological Survey
CLCD	China Land Cover Dataset
FVC	Fractional Vegetation Cover
NDVI	Normalized Difference Vegetation Index
GNDVI	Green Normalized Difference Vegetation Index
DVI	Difference Vegetation Index
MSAVI	Modified Soil Adjusted Vegetation Index
RVI	Ratio Vegetation Index
SAVI	Soil Adjusted Vegetation Index
PCA	Principal Component Analysis
RFR	Random Forest Regression
GBRT	Gradient Boosting Regression Tree
XGBoost	eXtreme Gradient Boosting

References

1. Lai, J.L.; Qi, S.; Chen, J.D.; Guo, J.C.; Wu, H.; Chen, Y.Z. Exploring the spatiotemporal variation of carbon storage on Hainan Island and its driving factors: Insights from InVEST, FLUS models, and machine learning. *Ecol. Indic.* **2025**, *172*, 113236. [CrossRef]

2. Leduc, F.; Coops, N.C.; Alexandre, M.B.; Guillaume, M.; Alexis, A. A Review of Dendrochronology and Remote Sensing Integration for Forest Growth and Disturbance Monitoring. *Curr. For. Rep.* **2025**, *11*, 25. [CrossRef]
3. Pan, Y.D.; Birdsey, R.A.; Phillips, O.L.; Houghton, R.A.; Fang, J.; Kauppi, P.E.; Keith, H.; Kurz, W.A.; Ito, A.; Lewis, S.L.; et al. The enduring world forest carbon sink. *Nature* **2024**, *631*, 563–569. [CrossRef]
4. Wang, X.Q.; Bu, Y.K.; Wei, J.T.; Zhao, P.X.; Liu, S.D. Spatio-temporal variation and driving forces of forest vegetation aboveground Carbon storage in Huanglong Mountain. *Acta Ecol. Sin.* **2023**, *43*, 7896–7909.
5. Ren, Z.B.; Zheng, H.F.; He, X.Y.; Zhang, D.; Shen, G.Q.; Zhai, C. Changes in spatio-temporal patterns of urban forest and its above-ground carbon storage: Implication for urban CO_2 emissions mitigation under China's rapid urban expansion and greening. *Environ. Int.* **2019**, *129*, 438–450. [CrossRef]
6. Liu, X.J.; Trogisch, S.; He, J.S.; Niklaus, P.A.; Bruelheide, H.; Tang, Z.Y.; Erfmeier, A.; Scherer-Lorenzen, M.; Pietsch, K.A.; Yang, B.; et al. Tree species richness increases ecosystem carbon storage in subtropical forests. *Proc. Biol. Sci.* **2018**, *285*, 20181240. [PubMed]
7. Maryam, P.; Shataee, S.; Mcroberts, R.E.; Mohammadi, J. Integrating airborne laser scanning data, space-borne radar data and digital aerial imagery to estimate aboveground carbon stock in Hyrcanian forests, Iran. *Remote Sens. Environ.* **2020**, *240*, 111669.
8. Zhang, M.; Du, H.Q.; Zhou, G.M.; Li, X.J.; Mao, F.J.; Dong, L.F.; Zheng, J.L.; Liu, H.; Huang, Z.H.; He, S.B. Estimating Forest Aboveground Carbon Storage in Hang-Jia-Hu Using Landsat TM/OLI Data and Random Forest Model. *Forests* **2019**, *10*, 1004. [CrossRef]
9. Kucuker, D.M.; Tuyoglu, O. Spatiotemporal patterns and driving factors of carbon dynamics in forest ecosystems: A case study from Turkey. *Integr. Environ. Assess. Manag.* **2022**, *18*, 209–223. [CrossRef]
10. Mngadi, M.; Odindi, J.; Onisimo, M. The Utility of Sentinel-2 Spectral Data in Quantifying Above-Ground Carbon Stock in an Urban Reforested Landscape. *Remote Sens.* **2021**, *13*, 4281. [CrossRef]
11. Junttila, V.; Minunno, F.; Peltoniemi, M.; Forsius, M.; Akujärvi, A.; Ojanen, P.; Mäkelä, A. Quantification of forest carbon flux and stock uncertainties under climate change and their use in regionally explicit decision making: Case study in Finland. *Ambio* **2023**, *52*, 1716–1733. [CrossRef] [PubMed]
12. Hao, W.L.; Li, Z.S.; Li, B.B. Dynamics and driving factors of soil organic carbon sequestration during vegetation restoration on Loess Plateau. *Bull. Soil Water Conserv.* **2025**, *45*, 233–241.
13. Li, R.W.; Han, G.D.; Sun, J.; Chi, W.F. Spatiotemporal Evolution and Coupling Evaluation of Ecosystem Services and Ecological Risks on the QinghaiXizang Plateau. *Chin. J. Grassland.* **2025**, *47*, 30–46.
14. Khan, S.N.; Li, D.; Maimaitijiang, M. A Geographically Weighted Random Forest Approach to Predict Corn Yield in the US Corn Belt. *Remote Sens.* **2022**, *14*, 2843. [CrossRef]
15. Ma, B.; Shen, H.; Feng, C.T.; Zhao, W.Y.; Wang, W. Assessing the integrated conservation effectiveness of protected areas on forest ecosystems in the Three Parallel Rivers Region, China. *Ecol. Indic.* **2025**, *178*, 113906. [CrossRef]
16. Wei, R.; Shu, Q.T.; Li, Z.Y.; Fu, L.J.; Xiang, Q.; Qin, C.G.; Rao, X.; Liu, J.F. Inversion of Grassland Aboveground Biomass in the Three Parallel Rivers Area Based on Genetic Programming Optimization Features and Machine Learning. *Remote Sens.* **2025**, *17*, 2936. [CrossRef]
17. *GB/T 38590-2020*; Technical Regulations for Continuous Forest Inventory. National Forestry and Grassland Administration: Beijing, China, 2020.
18. Liu, X.Y.; Zhang, M.L.; Ma, Z.M. Spatiotemporal Changes in Vegetation Cover and Analysis of Climatic Factors in Gansu Province from 1981 to 2020. *Huanjing Kexue* **2025**, *46*, 7831–7840. [PubMed]
19. Wang, T.; Zhang, C.; Zhou, H. Aboveground biomass estimation of major coniferous forests in Qujing City based on Landsat images. *J. Zhejiang AF Univ.* **2025**, *42*, 1132–1141.
20. Breiman, L. Random forests. *Mach. Learn.* **2001**, *45*, 5–32. [CrossRef]
21. Friedman, J.H. Greedy function approximation: A gradient boosting machine. *Ann. Stat.* **2001**, *29*, 1189–1232. [CrossRef]
22. Chen, T.Q.; Guestrin, C. XGBoost: A scalable tree boosting system. In Proceedings of the 22nd ACM SIGKDD International Conference on Knowledge Discovery and Data Mining, San Francisco, CA, USA, 13–17 August 2016; pp. 785–794.
23. Purwanto, P.; Utaya, S.; Handoyo, B.; Bachri, S.; Astuti, I.S.; Utomo, K.S.B.; Aldianto, Y.E. Spatio-temporal analysis of COVID-19 spread with emerging hotspot analysis and space-time cube models in east Java, Indonesia. *Int. J. Geo. Inf.* **2021**, *10*, 133.
24. Tan, M.H.; Xie, L.; Huang, Y.H.; Lu, H. Spatial and temporal characteristics and driving factors of urban heat island in Pinglu Canal Economic Belt, China. *J. Guangxi Norm. Univ. (Nat. Sci. Ed.)* **2026**, *44*, 185–198.
25. Wang, J.F.; Xu, C.D. Geodetector: Principle and prospective. *Acta Geogr. Sin.* **2017**, *72*, 116–134.
26. Yang, K.; Luo, K.; Zhang, J.L.; Qiu, B.; Wang, F.P.; Xiao, Q.L.; Cao, J.; He, Y.R.; Yang, J. Estimating forest aboveground carbon sink based on landsat time series and its response to climate change. *Sci. Rep.* **2025**, *15*, 589. [CrossRef] [PubMed]
27. Fang, J.Y.; Liu, G.H.; Xu, S.L. Biomass and net production of forest vegetation in China. *Acta Ecol. Sin.* **1996**, *16*, 497−508.
28. Kilbride, J.B.; Kennedy, R.E. A Large-Scale Inter-Comparison and Evaluation of Spatial Feature Engineering Strategies for Forest Aboveground Biomass Estimation Using Landsat Satellite Imagery. *Remote Sens.* **2024**, *16*, 4586. [CrossRef]

29. Marvin, D.C.; Asner, G.P.; Knapp, D.E.; Anderson, C.B.; Martin, R.E.; Sinca, F.; Tupayachi, R. Amazonian landscapes and the bias in field studies of forest structure and biomass. *Proc. Natl. Acad. Sci. USA* **2014**, *111*, E5224–E5232. [CrossRef] [PubMed]
30. Tijerín-Triviño, J.; Moreno-Fernández, D.; Zavala, M.A.; Astigarraga, J.; García, M. Identifying Forest Structural Types along an Aridity Gradient in Peninsular Spain: Integrating Low-Density LiDAR, Forest Inventory, and Aridity Index. *Remote Sens.* **2022**, *14*, 235. [CrossRef]
31. Tu, H.T.; Zhou, H.B.; Ma, G.Q.; Zhang, R.; Yang, S.Y. Characteristics of Forest Carbon Storage in Yunnan Based on the Ninth Forest Inventory Data. *J. North West For. Univ.* **2023**, *38*, 185–193.
32. Fan, H.P.; Liu, C.; Chen, F.Y. The Estimation of Forest Carbon Storage in Northwest Yunnan Based on Different Machine Learning Classification Algorithms. *J. Southwest For. Univ.* **2025**, *45*, 1–9.
33. Wang, F.; Xiang, S.Y.; Ren, J.T. Spatiotemporal Patterns and Evolutionary Trajectory of Terrestrial Ecosystem Carbon Storage in Southwest China from 1980 to 2020. *China Environ. Sci.* **2025**, *45*, 1–17.
34. Zhang, Y.C.; Hong, S.B.; Liu, D.; Piao, S.L. Susceptibility of vegetation low-growth to climate extremes on Tibetan Plateau. *Agric. For. Meteorol.* **2023**, *331*, 109323. [CrossRef]
35. Li, Y.F.; Mo, Y.H.; Qin, J.S.; Ma, J.M. Carbon Storage and Distribution Pattern of *Pinus massoniana* Plantations Ecosystem in Different Forest Ages in Guangxi. *Guangxi Sci.* **2024**, *31*, 346–356.
36. Guo, Y.; Wu, R.D.; Yang, F.L.; Wang, J.J. The spatial patterns of scenic spots in Three Parallel Rivers Region. *J. Yunnan Univ.* **2020**, *42*, 992–1003.
37. Wu, C.S.; Lu, R.R.; Zhang, P.; Dai, E.F. Multilevel ecological compensation policy design based on ecosystem service flow: A case study of carbon sequestration services in the Qinghai-Tibet Plateau. *Sci. Total Environ.* **2024**, *921*, 171093. [CrossRef]
38. Raich, J.W.; Russell, A.E.; Kitayama, K.; Parton, W.J.; Vitousek, P.M. Temperature influences carbon accumulation in moist tropical forests. *Ecology* **2006**, *87*, 76–87. [CrossRef]

Disclaimer/Publisher's Note: The statements, opinions and data contained in all publications are solely those of the individual author(s) and contributor(s) and not of MDPI and/or the editor(s). MDPI and/or the editor(s) disclaim responsibility for any injury to people or property resulting from any ideas, methods, instructions or products referred to in the content.